Nanoscale

Accepted Manuscript

This is an *Accepted Manuscript*, which has been through the Royal Society of Chemistry peer review process and has been accepted for publication.

Accepted Manuscripts are published online shortly after acceptance, before technical editing, formatting and proof reading. Using this free service, authors can make their results available to the community, in citable form, before we publish the edited article. We will replace this *Accepted Manuscript* with the edited and formatted *Advance Article* as soon as it is available.

You can find more information about *Accepted Manuscripts* in the **Information for Authors**.

ROYAL SOCIETY
OF CHEMISTRY

www.rsc.org/nanoscale

ARTICLE

Layer-modulated synthesis of uniform tungsten disulfide nanosheet using gas-phase precursors

Jusang Park+[a], Wonseon Lee+[a], Taejin Choi[a], Sung-Hwan Hwang[b], Jae Min Myoung[b], Jae-Hoon Jung[c], Soo-Hyun Kim[c] and Hyungjun Kim[a*]

The synthesis of layered transition-metal-disulfide (MS_2, M = Mo, W) nanosheets with layer controllability and large-area uniformity is an essential requirement for their application in electronic and optical devices. In this report, we describe a synthesis process of WS_2 nanosheets with layer controllability and high uniformity using chemical vapor deposition (CVD) and WCl_6 and H_2S as gas-phase precursors. Through this process, we can systematically modulate the thickness of WS_2 nanosheets by controlling the duration of the reaction between WCl_6 and H_2S. The CVD-grown WS_2 nanosheets exhibit good stoichiometry as well as dependencies of a clear Raman shift and bandgap on the number of layers. These properties are confirmed by X-ray photoemission spectroscopy, Raman spectroscopy, and photoluminescence measurements. The number of layers of WS_2 nanosheets is confirmed by atomic force microscopy. Finally, we demonstrate the fabrication and performance of a photodetector based on a hybrid structure consisting of graphene and a WS_2 nanosheet

Introduction

Recently, two-dimensional (2D) transition-metal disulfides (TMDs) have received much attention as new materials in logic circuits,[1] thin-film transistors,[2,3] sensors,[4,5] catalysts,[6–9] and optoelectronics.[10,11] Furthermore, the combination of 2D materials (heterostructures) has attracted scientific as well as technical interest in emerging applications.[12–16] Nanoflakes of transition-metal disulfide (MS_2, M = Mo, W) can be easily exfoliated from bulk MS_2 and transferred onto an arbitrary substrate using the scotch-tape method; this is feasible because MS_2 crystals are composed of sulfur –transition-metal–sulfur (S–M–S) layers that are stacked on top of each other by van der Waals interaction. Using this method, the physical, electrical, and optical properties of MS_2 have been intensively investigated[5,10,17–19] and found to depend significantly on thickness: while monolayered MS_2 has a direct bandgap, multilayered or bulk MS_2 has an indirect bandgap because of the broken symmetry in the atomic basis.[20] Moreover, the bandgaps of MS_2 nanosheets vary with thickness, resulting in thickness-dependent photodetection in a wide range of spectral responses.[10] Therefore, there is a critical need to synthesize thickness-modulated and uniform MS_2 nanosheets. Because mechanical exfoliation only produces small-sized flakes whose thickness cannot be controlled, considerable efforts have been devoted to synthesize MS_2-based materials, including sulfurization of metal[21] or metal-oxide[22,23] films and annealing with Mo- and S-containing solutions.[24] However, these

methods produce films with low carrier mobility (0.004–0.04 $cm^2V^{-1}s^{-1}$)[21] and they involve large complexity in the synthesis processes.[24] More recently, chemical vapor deposition (CVD) methods using WO_3 and MoO_3 with sulfur powder have been demonstrated.[25–27] Nanosheets of MoS_2 and WS_2 produced via this method show highly crystallinity and reasonable electrical properties;[25,26] however, this synthesis process still suffers from a lack of reliability since it is dominated by many process parameters that cannot be easily controlled, such as sulfur concentration, distance between the substrate and the crucible containing the S powder, and outgoing flow of gases from the chamber resulting in discontinuous and non-uniform nanosheets.[25,27] Consequently, an alternative approach is required to synthesize thickness-modulated and uniform nanosheets for future applications. We recently reported the synthesis of thickness-modulated WS_2 nanosheets using sulfurization methods with plasma-enhanced atomic layer deposition (PE-ALD) of WO_3 films, but successful use of direct deposition methods is not reported.

In this study, we developed a synthesis process with good thickness controllability and wafer-scale uniformity, through which single-, bi-, and multilayered WS_2 were systematically synthesized using the gas-phase CVD method. In particular, to more easily control the amount of precursors utilized, we used gas-phase precursors of WCl_6 and H_2S rather than WO_3 and S powders. The gas phase precursors only reported about the nanotube and nanoparticle [28] not nanosheet. With this strategy, we systematically modulated the thickness of WS_2 nanosheets

by controlling the reaction time between WCl$_6$ and H$_2$S. We analyzed WS$_2$ nanosheets of different thicknesses using optical microscopy (OM), Raman spectroscopy, high-resolution transmission electron microscopy (HRTEM), atomic force microscopy (AFM), and photoluminescence (PL) measurement. Furthermore, we demonstrated the fabrication and performance of a graphene–WS$_2$ hybrid photodetector.

Experimental

WS$_2$ Nanosheet Growth

For the synthesis of WS$_2$ nanosheets, SiO$_2$-coated Si wafers (referred to as SiO$_2$/Si substrates hereafter) were placed in the center of a tube furnace (3.05 cm/1.2 inch diameter). The temperature of the bubbler containing WCl$_6$ was kept at 100 °C to maintain an adequate vapor pressure, and gas-phase WCl$_6$ was transferred into the chamber by pure Ar (99.999 %) as the carrier gas.

Initially, the samples were heated to 700 °C for 30 min under flowing Ar gas (20 sccm) to remove organic contaminants on the surface. WCl$_6$ with a bubbling gas (Ar at 20 sccm) and H$_2$S were injected into the furnace at the same time, and the pressure of the chamber was maintained at 0.27 Torr during the process. At the end of the synthesis, the furnace was quickly cooled to room temperature under flowing Ar gas (20 sccm).

Transfer of WS$_2$ Nanosheets

The WS$_2$ nanosheets were covered with poly methyl methacrylate (PMMA) by spin coating at 2000 rpm for 30 s. After baking at 100 °C for 10 min, the samples were immersed in hydrofluoric acid for 1 s and then immersed in deionized water. Finally, the PMMA-coated WS$_2$ nanosheets on SiO$_2$/Si substrates were removed and allowed to dry under ambient air. After that, PMMA was washed away from the samples with acetone. To determine the crystallinity of the nanosheets, TEM measurements were obtained with a *Tecnai* G2 F20 S-TWIN at an acceleration voltage of 200 kV.

Graphene–WS$_2$ Hybrid Photodetector

Graphene was synthesized by CVD on a copper foil in a quartz tube furnace using a H$_2$–CH$_4$ gas mixture[29]. PMMA was then spin-coated onto the graphene/Cu substrate. The PMMA/graphene/Cu sample was placed in a container so that it floated on ammonium persulfate for 12 h in order to etch away the Cu foil. The resulting PMMA/graphene sample was then removed from the etch solution and was placed onto a CVD-grown monolayered WS$_2$ on a SiO$_2$/p++-Si substrate. The PMMA was removed with acetone and sample was then annealed at 300 °C for 3 h. We then fabricated source (S) and drain (D) electrodes using photolithography and lift-off processes, described as follows. First, photoresist (PR) layers were spin-coated on the sample. The substrate was then

exposed to ultraviolet (UV) light with a photomask to form the S/D electrode pattern. After the pattern was developed, we first deposited Au/Cr for the S/D electrodes with a thermal evaporation system. The lift-off process was then completed with an acetone rinse. In addition, we patterned graphene using photolithography and oxygen-plasma etching.

Results and Discussion
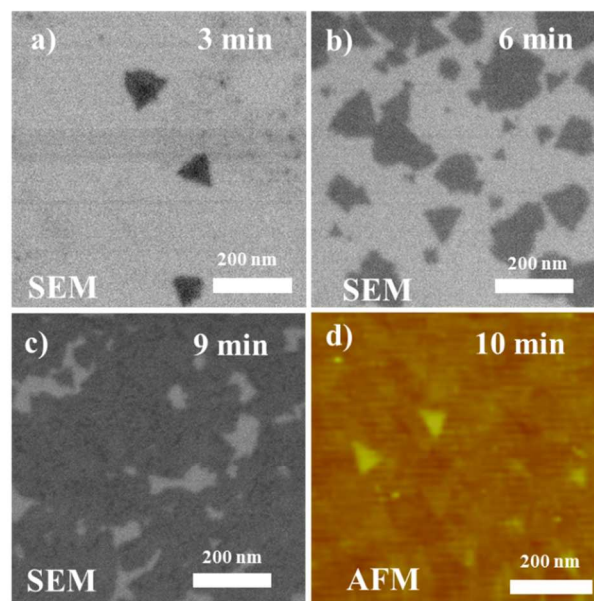
Fig. 1 (a–c) SEM images showing the growth process of a WS$_2$ nanosheet from small triangles to a continuous film. (d) AFM image showing the second monolayer growing on the first monolayer.

The initial growth of WS$_2$ nanosheets was observed as a function of time by a scanning electron microscope (SEM). In Fig. 1 a–c, the changes in the growth process are demonstrated by showing the most commonly observed features. Initially, small triangular domains about 100 nm in size nucleated at random locations on the substrate surface. The nucleation sites then continued to grow and formed boundaries when two or more domains met, resulting in a partially continuous film. When the growth time was sufficiently long, this process eventually produced a WS$_2$ nanosheet with a large area, as shown in Fig. 1c.[25] Fig. 1d. shows the nucleation of the second layer on the first monolayer, as observed by an AFM, which suggests a layer-by-layer growth mode of the WS$_2$ nanosheet.
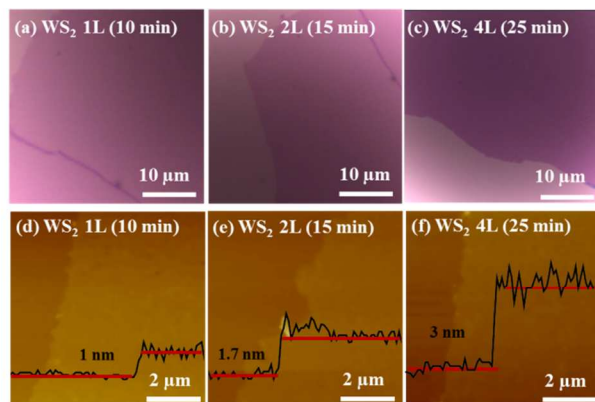
Fig. 2 OM images of WS_2 nanosheets transferred onto SiO_2 substrates for measurements of the (a) monolayer, (b) bilayer, and (c) tetralayer thickness. (d–f) Corresponding AFM images and inset height profiles of the transferred WS_2 nanosheets shown in (a–c).

Fig. 2a–c. show OM images of the synthesized WS_2 nanosheets after growth periods of 10, 15, and 25 min. The synthesized WS_2 nanosheets were uniform and continuous; the apparent colors of the transferred WS_2 nanosheets changed from pale violet to dark violet with increasing growth time. To confirm the thickness with AFM measurements, the WS_2 nanosheets were transferred to new SiO_2 substrates. Fig. 2d–f. show the AFM images of the transferred WS_2 nanosheets. The measured thicknesses of the synthesized WS_2 nanosheets were approximately 1 nm, 1.7 nm, and 3 nm for CVD durations of 10, 15, and 25 min, respectively. These thicknesses correspond to mono-, bi-, and tetralayers of WS_2 nanosheets, considering that the height of the WS_2 monolayer on SiO_2 was approximately 1 nm and the spacing between the first and the second WS_2 monolayers was approximately 0.65 nm.[27] The larger AFM-derived spacing between the first monolayer and the substrate is not surprising, since it involved distinct tip–sample and sample–substrate interactions. Similar effects have been observed in MoS_2 on graphene.[30–32] Thus, we conclude that the current WS_2 CVD process can systematically control the number of layers by controlling the growth time.
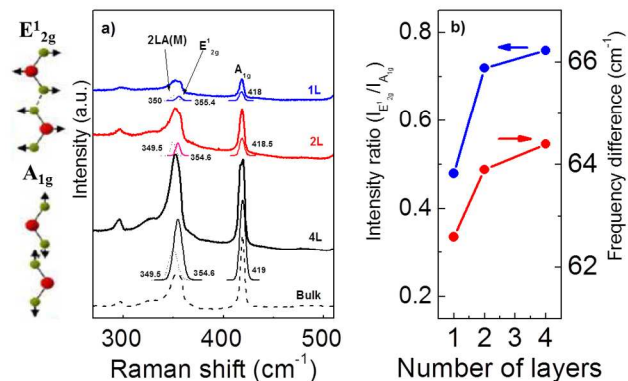
Fig. 3 (a) Raman spectra of the mono-, bi-, and tetralayered WS_2 nanosheets on SiO_2 substrates. (b) Relative Raman peak

intensities and peak distances of the E^1_{2g} and A^1_g modes of the mono-, bi-, and tetralayered WS_2 nanosheets.

The WS_2 nanosheets were further characterized using Raman spectroscopy, X-ray photoemission spectroscopy (XPS), and photoluminescence (PL) spectroscopy. The Raman spectra (excitation wavelength λ_{exc} = 633 nm) for the mono-, bi-, tetralayered and Bulk WS_2 nanosheets are shown in Fig. 3a. The first-order E^1_{2g} and A^1_g modes were observed, which correspond to in-plane and out-of-plane vibrations at 355.4 cm^{-1} and 418 cm^{-1}, respectively. In addition, the second-order mode was also observed, which corresponds to the second-order longitudinal acoustic mode, 2LA(M), at 350 cm^{-1}. It has been reported in detail that the changes in the ratio of the relative peak intensity, $I(E^1_{2g})/I(A^1_g)$, and peak distances between the E^1_{2g} and A^1_g modes depend on the number of layers (one, two, or four for mono-, bi-, or tetralayers, respectively, of WS_2).[33,34] To clearly check the agreement of the results with the those in the previous report, the Raman peaks were fitted using a Lorentzian function and the peak intensities and positions were extracted for the overlapping 2LA(M), and E^1_{2g} and A^1_g modes for different number of layers. Fig. 3b shows the relative-peak-intensity ratio and peak distance as functions of the number of layers. The value of the ratio increased from 0.5 to 0.76 as the number of layers increased from one to four, which was mainly affected by the scattering volume change.[34] The relative peak distance also increased from 62.6 cm^{-1} to 64.4 cm^{-1} with increasing number of layers owing to the increase in A^1_g-mode frequency and the decrease in E^1_{2g}-mode frequency. These variations in Raman frequency in the A^1_g and E^1_{2g} modes with the number of layers can be explained by the weak interlayer interaction and reduced long-range Coulomb interaction, respectively, between the effective charges caused by the increase in dielectric screening.[34,35]
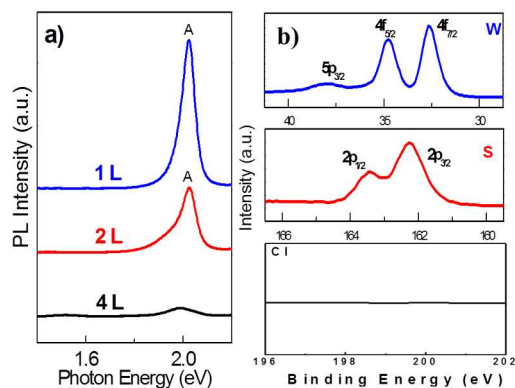
Fig. 4. (a) PL spectra of the mono-, bi-, and tetralayered WS_2 nanosheets on SiO_2 substrates. (b) XPS measurements of the W 4f, S 2p, and Cl 2p core levels of the monolayered WS_2 nanosheet.

The PL spectra of WS_2 with different number of layers are shown in Fig. 4a. The monolayered WS_2 exhibited a strong PL

signal at 2.01 eV, which is higher than any reported value for synthesized WS_2 but is consistent with the reported bandgap of monolayered WS_2.[33] A weak and wide PL signal was observed at 1.97 eV for the bilayered WS_2 nanosheet, while there was a very weak signal related to the tetralayered WS_2 nanosheet. The red shift and weakness of PL signals as the number of layers increased from one to two were due to the transition from a direct bandgap to an indirect one, which agrees well with previous results on the PL signals' dependence on the number of layers.[33,36,37] These PL results again confirm the layer controllability of the current process scheme.[33,36,37]

Fig. 4b shows the XPS of monolayered WS_2 nanosheets. The W 4f core-level spectrum shows three peaks at 34.8, 32.7, and 38.0 eV, which correspond to the W $4f_{5/2}$ and W $4f_{7/2}$ levels for W^{+4} and the W $5p_{3/2}$ state, respectively. The S 2p core-level spectrum exhibits two peaks at 163.5 and 162.3 eV, which correspond to the S $2p_{1/2}$ and S $2p_{3/2}$ states. The samples showed no Cl-related peaks, indicating the high purity of the film. Based on the XPS, the W to S ratio was calculated to be 2, indicating good stoichiometry of the WS_2 nanosheet.
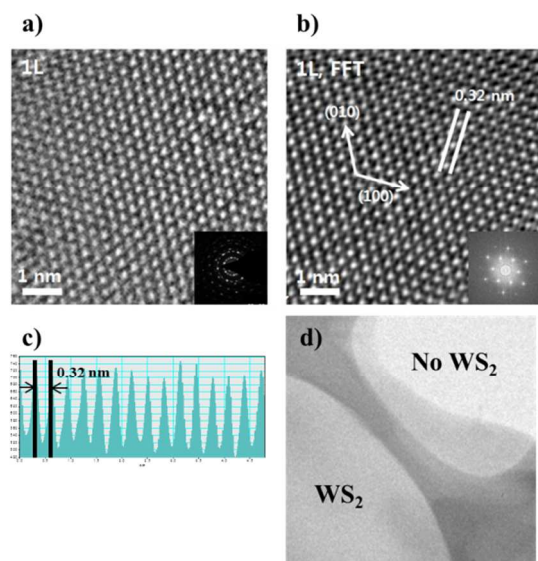
Fig. 5. (a) HRTEM image of a selected region on a monolayered WS_2 nanosheet. Inset: SAED pattern of the polycrystalline monolayered WS_2 nanosheet. (b) Atomic arrangement reconstructed by masking the FFT pattern from the inset. (c) Intensity profiles as indicated by the lines.

The crystallinity of the monolayered WS_2 nanosheet was analyzed by HRTEM. The HRTEM images in Fig. 5a–d. show periodically arranged atoms in a selected region of the monolayered WS_2. The selected-area electron diffraction (SAED) pattern in the inset of Fig. 5a indicates that the monolayered WS_2 had a polycrystalline structure. Fast Fourier transforms (FFTs) were conducted to obtain the original image of the WS_2 nanosheet's crystal structure (Fig. 5b), and six-fold coordination symmetry was clearly observed. To check the lattice constant of the WS_2 nanosheet, we performed inverse FFT by applying a mask. The lattice spacing (Fig. 5c) was

determined from the intensity profile to be 0.32 nm, which is consistent with the value shown in a previous report[11].
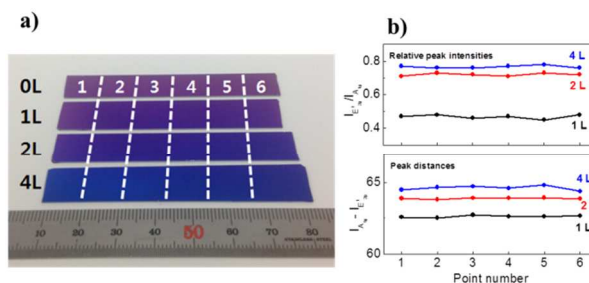
Fig. 6. (a) Large-area (1×7 cm^2) mono-, bi-, and tetralayered WS_2 nanosheets on SiO_2 substrates. (b) Raman spectra collected from six different areas of the mono-, bi-, and tetralayered WS_2 nanosheets on SiO_2 substrates.

Mono-, bi-, and tetralayered WS_2 were then synthesized on (1×7)-cm^2 SiO_2 substrates (Fig. 6a) to confirm the good and high uniformity of CVD-WS_2. The as-grown WS_2 nanosheets showed a distinct color depending on the number of layers. The Raman spectra were measured at six different positions along the length of the nanosheet to confirm its large-area uniformity. As shown in Fig. 6b, it can be seen that the peak positions of the 2LA(M) and the E^1_{2g} and A^1_g modes remain similar in all the spectra of the mono-, bi-, and tetralayered WS_2. The profiles of the Raman peaks, such as the full width at half maximum (FWHM) and the intensity, show negligible differences, as can be seen in Fig. 6b. This indicates that the synthesized thin film indeed possessed large-area uniformity over the (1×7)-cm^2 SiO_2 substrate.
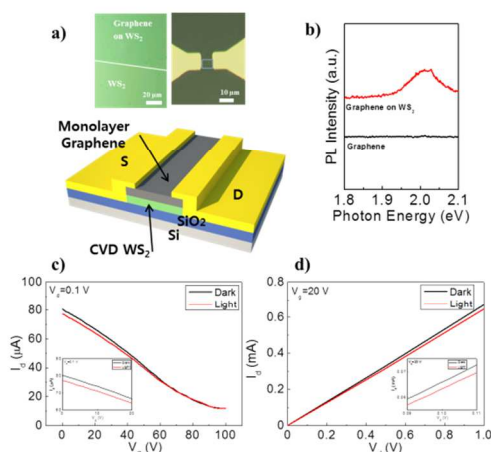
Fig. 7. (a) OM images of graphene on a WS_2 nanosheet and a graphene–WS_2 hybrid photodetector. (b) PL spectra of graphene on a WS_2 nanosheet and graphene only. (c) Source–drain current (I_d) versus backgate voltage (V_g) for graphene on WS_2 nanosheet in the absence and presence of light. Inset: I_d versus V_g from 0 to 20 V for graphene on WS_2 in the absence and presence of light. (d) I_d versus V_d for graphene on WS_2 in the absence and presence of light. Inset: I_d versus V_d from 0.09 to 0.11 V for graphene on WS_2 in the absence and presence of light.

In a previous study, an exceptional photoresponse from graphene–TMD heterostructures, with large quantum efficiency and photocurrent generation, was reported[30] mainly because of their large optical absorption (over 1×10^7 m^{-1}) and a visible range in the bandgap of TMDs. Thus, it would be interesting to evaluate the performance of photodetectors constructed with such materials. In particular, there has been no report on the photoresponse of CVD-synthesized-graphene–TMD heterostructures. Fig. 7a shows the top view of the graphene–WS_2 heterostructure produced simply by depositing graphene via CVD on a monolayered WS_2 nanosheet. Fig. 7a shows a clear difference in the optical contrast of graphene on the WS_2 nanosheet. The corresponding PL spectrum shows a PL signal at 2.02 eV, which is consistent with the monolayered WS_2 PL, as shown in Fig. 7b. Fig. 7c shows the source–drain current I_d between contacts located on graphene as a function of the backgate voltage V_g for a typical graphene–WS_2 hybrid device. The positive shift of the Dirac point was due to the luminescence of SiO_2 as a result of hole doping.[38] The device was then illuminated with a green light (wavelength = 550 nm). The red trace in Fig. 7c represents the variation in I_d with V_g when the device was illuminated continuously. The photocurrent (I_p) can be calculated from the difference between I_d, dark (80.6 μA) and I_d, light (77.44 μA) at V_g = 0 V and V_d = 0.1 V, and I_p = 3.16 μA was obtained. The negative sign of the photoconductivity at $V_g \ll V_{dirac}$ can be easily understood from the transfer of photoelectrons generated inside WS_2 to the graphene layer. However, the bands in WS_2 remained flat, suppressing the unidirectional transfer of electrons and equilibrating the charge distribution between graphene and WS_2. As shown in the insets of Fig. 7c and d, the ratio of the photocurrent and dark current (I_p/I_d, dark = 0.04) was lower than the ratio reported for graphene–exfoliated-MoS_2 owing to the trapped water between graphene and WS_2 from the graphene transfer process.[39] However, considering the large-area uniformity of the WS_2 nanosheet, we believe that the graphene–WS_2 hybrid photodetector is a promising candidate for a new class of scalable optoelectronic devices.

Conclusions

We have reported successful preparation of CVD-grown WS_2 using gas-phase precursors with WCl_6 and H_2S. The synthesis process of CVD-WS_2 nanosheets showed systematic layer controllability ranging from a monolayer to tetralayers by adjusting the growth time, thus improving the accessibility for fundamental research studies and industrial applications. Using AFM measurements, we calculated a growth rate of 5 min per layer; the initial growth mode was confirmed by SEM and AFM data as functions of synthesis time, where small triangular domains nucleated at random locations on the substrate, after which the nucleation sites continued to grow and formed boundaries when two or more domains met, resulting in a partially continuous film. The CVD-grown WS_2 nanosheet exhibited Raman shift and bandgap shift that depended on the

number of layers and their good qualities were demonstrated in the PL, XPS, and TEM results. It was confirmed that the WS2 nanosheet was deposited in mono-, bi-, and tetralayers on large-area (1×7 cm^2) SiO_2 substrates. Furthermore, we fabricated a graphene–WS_2 hybrid photodetector and evaluated its properties, which show the possibility of its application in optoelectronics. Our work is proof that gas-phase CVD will provide a foundation to further develop processes for the synthesis of TMD nanosheets.

Notes and references

a School of Electrical and Electronics Engineering, Yonsei University, 262 Seongsanno, Seodaemun-gu, Seoul, 120-749, Republic of Korea
b Department of Materials Science and Engineering, Yonsei University, 262 Seongsanno, Seodaemun-gu, Seoul, 120-749, Republic of Korea
c Nano-Devices and Process Laboratory, School of Materials Science and Engineering, Yeungnam University, Dae-Dong, Gyeongsan-Si 712-749, Republic of Korea.
† These authors contributed equally.
* To whom correspondence should be addressed. E-mail: hyungjun@yonsei.ac.kr

1. H. Wang, L. Yu, Y.-H. Lee, Y. Shi, A. Hsu, M. L. Chin, L.-J. Li, M. Dubey, J. Kong, and T. Palacios, Nano Lett., 2012, **12**, 4674.
2. S. Kim, A. Konar, W.-S. Hwang, J. H. Lee, J. Lee, J. Yang, C. Jung, H. Kim, J.-B. Yoo, J.-Y. Choi, Y. W. Jin, S. Y. Lee, D. Jena, W. Choi and K. Kim, Nat. Commun., 2012, **3**, 1011.
3. B. Radisavljevic, A. Radenovic, J. Brivio, V. Giacometti and A. Kis, Nature Nanotech., 2011, **6**, 147.
4. F. K. Perkins, A. L. Friedman, E. Cobas, P. M. Campbell, G. G. Jernigan and B. T. Jonker, Nano Lett., 2013, **13**, 668.
5. H. Li, Z. Yin, Q. He, H. Li, X. Huang, G. Lu, D. W. H. Fam, A. I. Y. Tok, Q. Zhang and H. Zhang, Small, 2012, **8**, 63.
6. D. Voiry, H. Yamaguchi, J. Li, R. Silva, D. C. B. Alves, T. Fujita, M. Chen, T. Asefa, V. B. Shenoy, G. Eda and M. Chhowalla, Nature Mater., 2013, **12**, 850.
7. Y. Yu, S.-Y. Huang, Y. Li, S. N. Steinmann, W. Yang and L. Cao, Nano Lett., 2014, **14**, 553.
8. R. Bhandavat, L. David, and G. Singh, J. Phys. Chem. Lett. 2012, **3**, 1523−1530.
9. J. Kibsgaard, Z. Chen, B. N. Reinecke and T. F. Jaramillo, Nature Mater., 2012, **11**, 963.
10. H. S. Lee, S.-W. Min, Y.-G. Chang, M. K. Park, T. Nam, H. Kim, J. H. Kim, S. Ryu and S. Im, Nano Lett., 2012, **12**, 3695.

11. N. Perea-López, A. L. Elías, A. Berkdemir, A. Castro-Beltran, H. R. Gutiérrez, S. Feng, R. Lv, T. Hayashi, F. López-Urías, S. Ghosh, B. Muchharla, S. Talapatra, H. Terrones and M. Terrones, Adv. Funct. Mater., 2013, **23**, 5510.

12. K. Kośmider and J. Fernández-Rossier, Phys. Rev. B, 2013, **87**, 075451.

13. L. Britnell, R. V. Gorbachev, R. Jalil, B. D. Belle, F. Schedin, A. Mishchenko,T. Georgiou, M. I. Katsnelson, L. Eaves, S. V. Morozov, N. M. R. Peres, J. Leist, A. K. Geim, K. S. Novoselov and L. A. Ponomarenko, Science, 2012, **335**, 947.

14. K. S. Novoselov and A. H. Castro Neto, Phys. Scr., 2012, **T146**, 014006.

15. G.-H.Lee, Y.-J. Yu, X. Cui, N. Petrone, C.-H. Lee, M. S. Choi, D.-Y. Lee, C. Lee, W. J. Yoo, K. Watanabe, T. Taniguchi, C. Nuckolls, P. Kim and J. Hone, ACS Nano, 2013, **7**, 7931.

16. T. Georgiou, R. Jalil, B. D. Belle, L. Britnell, R. V. Gorbachev, S. V. Morozov, Y.-J. Kim, A. Gholinia, S. J. Haigh, O. Makarovsky, L. Eaves, L. A. Ponomarenko, A. K. Geim, K. S. Novoselov and A. Mishchenko, Nature Nanotech., 2013, **8**, 100.

17. J. S. Ross, S. Wu, H. Yu, N. J. Ghimire, A. M. Jones, G. Aivazian, J. Yan, D. G. Mandrus, D. Xiao, W. Yao and X. Xu, Nat Commun., 2013, **4**, 1474.

18. B. W. H. Baugher, H. O. H. Churchill, Y. Yang and P. Jarillo-Herrero, Nano Lett., 2013, **13**, 4212.

19. Y. Li, C.-Y. Xu and L. Zhen, Appl. Phys. Lett., 2013, **102**, 143110.

20. J. Kang, S. Tongay, J. Zhou, J. Li and J. Wu, Appl. Phys. Lett., 2013, **102**, 012111.

21. Y. Zhan, Z. Liu, S. Najmaei, P. M. Ajayan and J. Lou, Small, 2012, **8**, 966.

22. A. L. Elías, N. Perea-López, A. Castro-Beltrán, A. Berkdemir, R. Lv, S. Feng, A. D. Long, T. Hayashi, Y. A. Kim, M. Endo, H. R. Gutiérrez, N. R. Pradhan, L. Balicas, T. E. Mallouk, F. López-Urías, H. Terrones and M. Terrones, ACS Nano, 2013, **7**, 5235.

23. R. Morrish, T. Haak, and C. A. Wolden, Chem. Mater. 2014, **26**, 3986−3992

24. K.-K. Liu, W. Zhang, Y.-H. Lee, Y.-C. Lin, M.-T. Chang, C.-Y. Su, C.-S. Chang, H. Li, Y. Shi, H. Zhang, C.-S. Lai and L.-J.Li, Nano Lett., 2012, **12**, 1538.

25. S. Najmaei, Z. Liu, W. Zhou, X. Zou, G. Shi, S. Lei, B. I. Yakobson, J.-C. Idrobo, P. M. Ajayan and J. Lou, Nature Mater., 2013, **12**, 754.

26. A.M. van der Zande, P. Y. Huang, D. A. Chenet, T. C. Berkelbach, Y. You, G.-H. Lee, T. F. Heinz, D. R. Reichman, D. A. Muller and J. C. Hone, Nature Mater., 2013, **12**, 554.

27. Y.-H. Lee, L. Yu, H. Wang, W. Fang, X. Ling, Y. Shi, C.-T. Lin, J.-K. Huang, M.-T. Chang, C.-S. Chang, M. Dresselhaus, T. Palacios, L.-J. Li and J. Kong, Nano Lett., 2013, **13**, 1852.

28. A. Margolim, F. L. Deepak, R. Popovitz-Biro, M Bar-adan, Y. Feldman and R. Tenne, Nanotechnology, 2008, **19**, 095601.

29. L. David, R. Bhandavat, G. Kulkarni, S. Pahwa, Z. Zhong, and G. Singh, ACS Appl. Mater. Interfaces, 2013, **5**, 546−552.

30. L. Britnell, R. M. Ribeiro, A. Eckmann, R. Jalil, B. D. Belle, A. Mishchenko, Y.-J. Kim, R. V. Gorbachev, T. Georgiou, S. V. Morozov, A. N. Grigorenko, A. K. Geim, C. Casiraghi, A. H. Castro Neto and K. S. Novoselov, Science, 2013, **340**, 1311.

31. G. Eda, H. Yamaguchi, D. Voiry, T. Fujita, M. Chen and M. Chhowalla, Nano Lett., 2011, **11**, 5111.

32. A. Gupta, G. Chen, P. Joshi, S. Tadigadapa and P. C. Eklund, Nano Lett., 2006, **6**, 2667.

33. H. R. Gutiérrez, N. Perea-López, A. L. Elías, A. Berkdemir, B. Wang, R. Lv, F. López-Urías, V. H. Crespi, H. Terrones and M. Terrones, Nano Lett., 2012, **13**, 3447.

34. A. Berkdemir, H. R. Gutiérrez, A. R. Botello-Méndez, N. Perea-López, A. L. Elías, C.-I. Chia, B. Wang, V. H. Crespi, F. López-Urías, J.-C. Charlier, H. Terrones and M. Terrones, Sci. Rep., 2013, **3**, 1755.

35. A. Molina-Sánchez and L. Wirtz, Phys. Rev. B, 2011, **84**, 155413.

36. W. Zhao, Z. Ghorannevis, L. Chu, M. Toh, C. Kloc, P.-H. Tan and G. Eda, ACS Nano, 2012, **7**, 791.

37. H. Zeng, G.-B. Liu, J Dai, Y. Yan, B. Zhu, R. He, L. Xie, S. Xu, X. Chen, W. Yao and X. Cui, Sci. Rep., 2013, **3**, 1608.

38. S. Ryu, L. Liu, S. Berciaud, Y.-J. Yu, H. Liu, P. Kim, G. W. Flynn and L. E. Brus, Nano Lett., 2010, **10**, 4944.

39. K. Roy, M. Padmanabhan, S. Goswami, T. P. Sai, G. Ramalingam, S. Raghavan and A. Ghosh, Nature Nanotech., 2013, **8**, 826.